

Synthesis, Characterization and Enhanced Photocatalytic Activity of Iron Oxide/Carbon Nanotube/Ag-doped TiO₂ Nanocomposites

*José O. Marques Neto,^a Carlos R. Bellato,^{*a} Carlos H. F. de Souza,^a
Renê C. da Silva^b and Pablo A. Rocha^c*

^aDepartamento de Química, ^bDepartamento de Física and ^cDepartamento de Solos,
Universidade Federal de Viçosa (UFV), 36570-900 Viçosa-MG, Brazil

A novel magnetically recoverable catalyst (Fe/MWCNT/TiO₂-Ag) was prepared in this study by a process that involves few steps. Titanium dioxide doped with silver and iron oxide was deposited on support of multi-walled carbon nanotubes (MWCNT). The synthesized catalysts were characterized by inductively coupled plasma mass spectrometry (ICP-MS), N₂ adsorption/desorption, X-ray diffraction (XRD), scanning electron microscopy (SEM), energy dispersive spectrometry (EDS), infrared spectroscopy (IR) and UV-Vis diffuse reflectance spectra (DRS). Phenol in aqueous solution (50 mg L⁻¹) was used as a model compound for evaluation of UV-Vis (filter cut off for $\lambda > 300$ nm) photocatalytic activity. The composite catalyst has a high photocatalytic activity, destroying ca. 100% of phenol and removing 85% of total organic carbon in an aqueous solution after 180 min. The Fe/MWCNT/TiO₂-Ag catalyst remained stable, presenting an 8% decrease in phenol degradation efficiency after ten consecutive photocatalytic cycles.

Keywords: visible light, photocatalysis, titanium dioxide, magnetic separation, phenol

Introduction

Among the semiconductors used in heterogeneous photocatalysis, titanium dioxide is that most used due to specific properties, including high photosensitivity, non-toxic nature, chemical stability and relatively low cost.^{1,2} One inherent problem to the use of this catalyst is the electron-hole recombination and its high band-gap value of 3.2 eV, limiting its photoactivity at low wavelengths and preventing the use of TiO₂ in applications with visible light.^{3,4}

Doping of TiO₂ with metals such as gold, platinum, rhodium and silver increases the spectrum of radiation absorption by TiO₂, allowing for its use with visible light.⁵ Silver has a low cost when compared to other noble metals and has electronic properties that make it a good option for use as a dopant on the surface of TiO₂. The working function of silver (4.26 eV) lies below the conduction band (CB) of TiO₂ (4.20 eV), Au (4.8 eV) and Pt (5.3 eV), and therefore silver can capture the photogenerated electrons of TiO₂, acting as electron traps and avoiding the recombination of the hole-electron pairs.⁶⁻⁸

The use of carbon nanotubes as support materials can provide functional properties, such as increase of the

specific surface area, high mechanic strength and high conductivity due to their remarkable electrochemical properties.⁹ Carbon nanotubes have high electron storage capacity and may thereby receive the photogenerated electrons from the TiO₂ CB.¹⁰ The carbon nanotubes when in contact with TiO₂ alter its absorption of radiation to longer wavelength light (visible light) due to $\pi \rightarrow \pi^*$ transitions of the nanotubes and $n \rightarrow \pi^*$ between the n orbitals of the oxygen of TiO₂ and π^* of the nanotubes.¹¹ These unique characteristics of multi-walled carbon nanotubes (MWCNT) have attracted the attention of many researchers in the preparation of nanocomposites with TiO₂. The MWCNT properties contribute to facilitate the load transfer, functioning as electron acceptors.¹²

The incorporation of magnetic properties of iron oxides such as magnetite or maghemite in TiO₂-based catalysts facilitates its removal from the aqueous solution by application of an appropriate magnetic field, reducing costs and time spent in the extraction of the catalyst to permit its recycling.^{13,14}

In addition to its magnetic properties, the iron oxide creates additional energy levels to capture electrons from the conduction band and holes from the valence band of TiO₂, promoting a more effective separation of charges and reducing electronic recombination.¹⁵

*e-mail: bellato@ufv.br

Several studies have been performed using TiO₂ based catalysts with magnetic properties. Zhou *et al.*¹⁴ prepared MWCNT/Fe₃O₄/TiO₂ photocatalyst by *in situ* polymerization with polyacrylic acid and applied it in the phenol photodegradation with UV-Vis light. Luo *et al.*¹⁶ fabricated a TiO₂/Fe₃O₄/MWCNT magnetic catalyst by polymerization method using pyrrole as a support. Zhang *et al.*¹⁷ synthesized the TiO₂/Fe₃O₄/MWNTs catalyst by *in situ* hydrolysis method and applied for degradation of methylene blue under UV light. Aguilar *et al.*¹⁸ prepared TiO₂-Fe₃O₄-Ag catalyst doped with silver or gold and evaluated the effectiveness for phenol degradation with UV light and visible light.

There are no reports in the literature on the photocatalytic properties of Fe/MWCNT/TiO₂-Ag composites. In this work, we evaluated the effect of the interaction between iron oxide, silver and MWCNT with regards to the increase of the TiO₂ photocatalytic activity, allowing its application with UV-Vis light (cut off filter for $\lambda > 300$ nm). In this study, a new magnetically recoverable composite of TiO₂ doped with silver and iron oxide and impregnated on multi-walled carbon nanotubes (10-Fe/MWCNT/TiO₂-Ag-9) was synthesized by a facile method that involves only a few steps. Furthermore, silver, iron oxide and MWCNT interact with TiO₂, thus improving its efficiency for photodegradation of organic compounds. The effect of varying wt.% of Ag and Fe and MWCNT:TiO₂-Ag wt. ratio on the Fe/MWCNT/TiO₂-Ag composite was evaluated with regards to phenol photodegradation. Phenol is a common organic pollutant in the environment with high toxicity and carcinogenicity, structural stability and resistance to biodegradation.¹⁹

Experimental

Materials

MWCNT were used as received with purity > 93%, outer diameter between 10 and 50 nm and estimated length of 5 to 30 μ m, produced in the Laboratory of Nanomaterials, Physics Department, at Universidade Federal de Minas Gerais (UFMG), Brazil. The TiO₂ used was P25, acquired from Degussa, consisting of 80% anatase and 20% rutile. The commercial reagents silver nitrate, ethylene glycol, isopropyl alcohol and phenol were obtained from Sigma-Aldrich. All solutions were prepared with analytical grade reagents and high purity deionized water produced by a Milli-Q[®] system (Millipore, Bedford, MA, USA).

Preparation of iron oxide

A solution containing 1.6 L of water, 2.0 g of FeCl₃·6H₂O and 4.8 g of FeSO₄·7H₂O was heated to 70 °C.

Next, 120 mL of a solution of 5 mol L⁻¹ NaOH were added to the solution containing Fe salts, causing iron oxide precipitation. The obtained solid was washed with water to pH 7.0 and then dried at 70 °C for 18 h.²⁰

Preparation of the Fe/MWCNT/TiO₂-Ag catalyst

The silver nanoparticles (Ag NPs) were deposited on the surface of the commercial TiO₂ (Degussa P25) according to the photodeposition method, in which Ag⁺ ions were converted to Ag NPs in the presence of oxalic acid and UV-Vis irradiation.²¹ The products were designated as TiO₂-Ag-X, in which X indicates the contents of Ag. The X values in our experiments were 1.0, 2.0, 4.0, 6.0, 9.0, 15.0 and 20.0 wt.%.

Samples consisting of 20 mg of TiO₂-Ag-X were added to 100 mL of water and stirred for 20 min. Next, 10 mg of MWCNT were added and stirring continued for 30 min. Isopropyl alcohol was then added in the concentration of 50 mL *per* 30 mg of MWCNT followed by stirring for 30 min, and ethylene glycol was dispersed at the concentration of 15 mL *per* 30 mg of MWCNT.^{22,23} The resulting suspension remained under agitation for 6 h and was then filtered, washed with distilled water and the obtained solid (MWCNT/TiO₂-Ag-X) was dried in an oven at 70 °C. The TiO₂-Ag in the catalyst was studied varying their quantity *per* g of MWCNT. The weight ratio of MWCNT:TiO₂-Ag was varied to 1:1, 1:1.5, 1:2, 1:3 and 1:4, and Ag wt.% was maintained fixed at 9%. The obtained catalysts were labeled as Y-MWCNT/TiO₂-Ag, where Y = 11, 11.5, 12, 13 and 14 wt. ratio MWCNT:TiO₂-Ag.

The Fe/MWCNT/TiO₂-Ag composite was obtained by adding 1 g of 12-MWCNT/TiO₂-Ag-9 to 500 mL of water. To this suspension, different amounts of iron oxide were added. The suspension was maintained under stirring for 2 h, filtered, washed with distilled water and dried in an oven at 70 °C. The magnetically recoverable catalysts were labeled as Z-Fe/MWCNT/TiO₂-Ag-9, where Z = 5.0, 10.0, 15.0, 20.0 and 25.0 wt.% of Fe.

Photocatalyst characterization

The determination of the final photocatalyst chemical compositions was made by mixing 0.100 g of each sample with 3 mL of HNO₃ (65%), 4 mL of H₂SO₄ (96%), 4 mL of HCl (37%) and 1 mL of HF (40%), followed by digestion in an industrial microwave oven (Milestone Ethos) by heating to 230 °C for 15 min and maintaining this temperature for 20 min at 1,200 W. The digested samples were diluted and metal concentrations were determined by inductively

coupled plasma mass spectrometry (ICP-MS), PerkinElmer model NexION 300D.

The textural properties of the samples were analyzed by their N₂ adsorption-desorption isotherms using a surface area and pore size analyzer (NOVA 2200e Quanta Chrome Instruments, Boynton Beach, FL, USA). Prior to measurement, the samples were degassed at 110 °C for 4 h. Specific surface areas were estimated by the Brunauer-Emmett-Teller (BET) method and pore volumes were determined by the Horváth-Kawasoie (HK) method applied to the desorption branch.

X-ray diffraction (XRD) was measured by 2 θ scans utilizing a Bruker model D8 Discover diffractometer using Cu K α radiation ($\lambda = 0.1541$ nm) with an angular variation of 5-80° (2 θ) and scan rate of 0.05 degree s⁻¹. The Powder Diffraction File (PDF) database (JCPDS, International Centre for Diffraction Data) was used to identify crystalline phases. Network parameters (d_{hkl}) of the composites were calculated according to the Bragg equation, $\lambda = 2d \sin \theta$, where λ is the wavelength of X-rays ($\lambda = 0.1541$ nm) and θ is the diffraction angle.²⁴

Scanning electron microscopy (SEM) images were obtained using a JEOL JSM-6010/LA microscope. The SEM equipment was equipped with an energy dispersive spectrometry system (EDS) for analysis of the sample chemical composition.

Infrared spectra (IR) were obtained using a VARIAN 660-IR spectrophotometer equipped with an attenuated reflectance accessory PIKE Gladi ATR in the region of 400 to 4000 cm⁻¹.

Diffuse reflectance spectra (DRS) were acquired on a dual-beam 20 GBC, Cintra model spectrophotometer, in the region of 350-700 nm. Calcium carbonate was used as a non-absorbing standard.

Total organic carbon (TOC) was measured using a Shimadzu-5000A TOC analyzer.

In order to detect the presence of TiO₂ and iron oxide in the catalysts, analyses were also conducted by Raman scattering, using a Renishaw Raman Invia micro spectrometer equipped with an argon laser (514.5 nm) with a 50 × objective (NA = 0.75, corresponding to a spot of ca. 1 μ m in diameter) and spectral resolution of 1 cm⁻¹.

The zeta potential of adsorbents was measured using the Zetasizer Nano ZS instrument at pH values from 2 to 8.

Photocatalytic activity

The photocatalytic activity of the Fe/MWCNT/TiO₂-Ag composites was assessed by photodegradation of a phenol solution in an annular photoreactor (Figure S1 in the Supplementary Information (SI) section). The composites

and phenol solution were stirred for 15 min in the dark and then irradiated by UV-Vis light (filter cut off for $\lambda > 300$ nm) for 180 min. At established time intervals, aliquots were taken from samples, and filtered through a 0.45 μ M membrane (Millipore) for phenol and total organic carbon (TOC) quantification. The monitoring of the remaining phenol concentrations was carried out by high performance liquid chromatography (HPLC) using a 1260 Infinity system with a linear photodiode array detector (DAD) (Agilent Technologies). The chromatographic conditions used for quantification of phenol by HPLC-DAD are described by Almeida *et al.*²⁵

Photolysis was evaluated under the same conditions without the presence of the catalyst and only UV-Vis light. All studies were performed in triplicate.

Reuse assays

Photocatalysts were washed with deionized water and dried before reuse. The photocatalysts were characterized by X-ray diffraction techniques and infrared spectroscopy before and after each photodegradation cycle to verify its stability.

Results and Discussion

Scanning electron microscopy, energy dispersive spectroscopy and chemical composition

Surface analysis of the materials by SEM is shown in Figure S2 (in the SI section). Figure S2a shows the carbon nanotubes. In Figures S2b and S2c, the presence of dispersed granules of TiO₂-Ag and/or iron oxide along the surface of the carbon nanotubes is observed.^{26,27} The image of the material after ten consecutive reutilization cycles (Figure S2d) presents morphology similar to that of the unused material, thus confirming maintenance of the material structure. Figure S3 (in the SI section) shows the elemental analysis results of EDS spectra. The presences of Ti, Ag and Fe peaks are observed in the spectra. The spectrum of Figure S3d is similar to that of Figure S3c, indicating that the structure of the catalyst was not altered after ten reuse cycles.

Table 1 shows the quantities determined by ICP-MS of the Ti, Ag and Fe metals in the composites making up the catalysts. It can be observed that the quantities of each metal in the catalyst were close to the values initially calculated.

Specific surface area

The pore surface area and pore volume of the (Table 1) MWCNT/TiO₂-Ag-9 and 10-Fe/MWCNT/TiO₂-Ag-9

Table 1. Initial and final chemical compositions, final mass ratios, band-gap values and textural analysis of the synthesized photocatalysts

Sample	Ratio (wt.)						Metal loading / wt. %				Band gap / eV	S _{BET} ^a / (m ² g ⁻¹)	Pore volume / (cm ³ g ⁻¹)
	Initial			Final			Initial		Final				
	Ag:Ti	Fe:Ti	Fe:Ag:Ti	Ag:Ti	Fe:Ti	Fe:Ag:Ti	Ag	Fe	Ag	Fe			
MWCNT	–	–	–	–	–	–	–	–	–	–	–	95.5	0.0344
TiO ₂	–	–	–	–	–	–	–	–	–	–	3.20	48.0	0.0178
TiO ₂ -Ag-9	1:7	–	–	1:6.9	–	–	9.0	–	8.4	–	3.05	55.7	0.0203
MWCNT/TiO ₂ -Ag-9	1:7	–	–	1:6.8	–	–	9.0	–	8.2	–	2.84	64.7	0.0235
10-Fe/MWCNT/TiO ₂	1:7	1:6	–	–	1:6	–	–	10	–	9.5	2.52	60.7	0.0223
10-Fe/MWCNT/TiO ₂ -Ag-9	1:7	1:6	1:1.2:7	1:6.9	1:5.8	1:1.1:6.9	9.0	10	8.6	9.8	2.24	68.8	0.0253

^aS_{BET}: specific surface area.

catalysts are greater than those of TiO₂ and TiO₂-Ag-9. The introduction of MWCNT in the catalysts prevents the TiO₂ particle agglomerations, increasing the surface area.²⁸ The SEM images reinforce this fact, showing that the TiO₂-Ag and/or iron oxide particles were dispersed on the surface of MWCNTs.

X-ray diffraction

The diffractograms obtained for the X-ray diffraction patterns of the samples are shown in Figure 1. The peaks corresponding to the carbon nanotubes (Figure 1a) appear at 26.10° and 44.70°, and correspond to the diffraction planes (002) and (100).^{28,29} Regarding the diffractogram of iron oxide (Figure 1b), characteristic peaks of magnetite and maghemite are observed, being indistinguishable by XRD.³⁰ The main peaks of magnetite-maghemite were observed at 30.10°, 35.50°, 43.10°, 53.40°, 57.04° and 62.88°, representing the diffraction planes (220), (311), (400), (422), (511) and (440), respectively.^{31–33} The diffractogram in Figure 1c shows the main peaks for TiO₂. The peaks are labeled A (hkl) or R (hkl) related to the anatase (JCPDS file No. 21-1272) or rutile (JCPDS file No. 21-1276) phases, respectively, and agree with the crystallographic standards found in the literature.^{34–36} The X-ray diffraction patterns of TiO₂-Ag (Figure 1d) exhibit characteristic peaks of metallic silver (Ag⁰). However, the largest peak that reveals the crystalline structure of silver appears at 38.20° referring to the plane (111) superimposed on the peak 37.80° (004) of the TiO₂ anatase phase.³⁷ Silver (Ag⁺) has an ionic radius of 0.126 nm, greater than Ti⁴⁺ (0.068 nm), making impossible its substitution in the crystalline structure of TiO₂, but permitting only the impregnation on the TiO₂ surface.³⁸

The diffractogram of 10-Fe/MWCNT/TiO₂-Ag-9 is not altered when compared to the precursors, MWCNT, iron oxide and nano-TiO₂. There was only the overlapping of

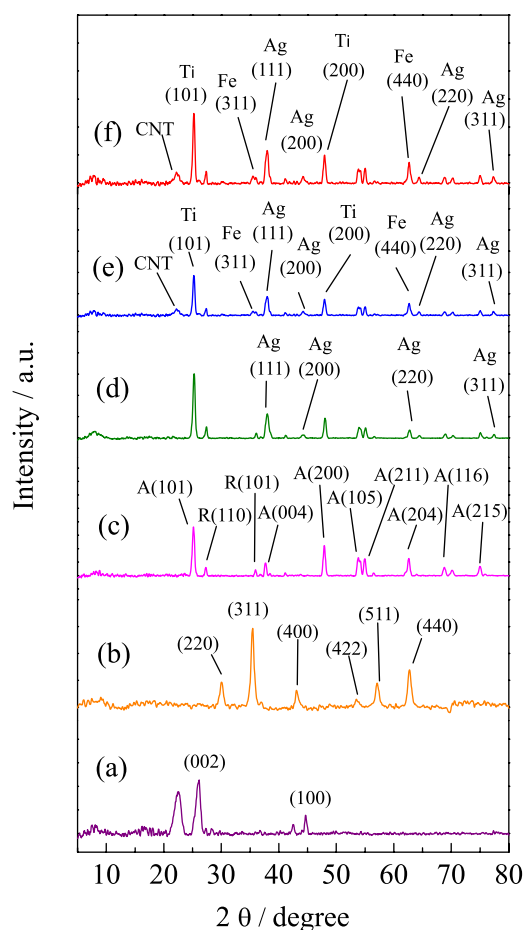


Figure 1. X-ray diffraction patterns of (a) MWCNT, (b) magnetic iron oxide, (c) TiO₂, (d) TiO₂-Ag-9, (e) 10-Fe/MWCNT/TiO₂-Ag-9 and (f) 10-Fe/MWCNT/TiO₂-Ag-9 (reused).

the peaks, and this demonstrates that the combination of iron oxide, TiO₂ and MWCNT is likely a physical process.

Infrared spectroscopy analysis

Figure 2a shows the obtained spectrum for TiO₂ nanoparticles, in which there is an absorption band in the

low frequency region ($400\text{--}800\text{ cm}^{-1}$), which is associated to the Ti–O vibration mode from the structure of Ti–O–Ti bonds. The spectrum obtained for the carbon nanotubes (Figure 2b) shows the presence of C=C stretching bands at 1580 cm^{-1} and C–C at 2340 cm^{-1} .^{39,40}

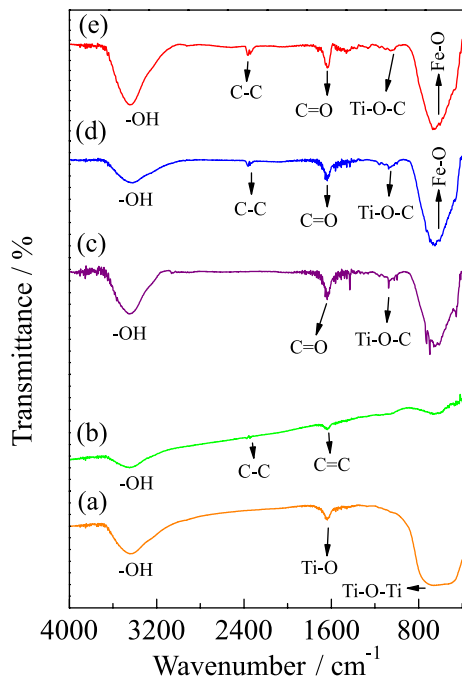


Figure 2. Infrared spectra of (a) TiO₂, (b) MWCNT, (c) MWCNT/TiO₂-Ag-9, (d) 10-Fe/MWCNT/TiO₂-Ag-9 and (e) 10-Fe/MWCNT/TiO₂-Ag-9 (reused).

The spectra of Figures 2d and 2e show the presence of bands at 572 and 628 cm^{-1} characteristic of the Fe–O bond of the magnetic iron oxide.⁴¹ In the spectra of Figures 2c–2e, a stretching of the Ti–O–C bond at 1065 cm^{-1} is observed, confirming the bond of TiO₂ to the carbon nanotube structures.⁴²

Raman spectroscopy

Figure 3 shows the Raman spectrum of the synthesized catalysts. The Raman spectrum of iron oxide (Figure 3a) shows a broad band from $670\text{--}720\text{ cm}^{-1}$ associated to magnetite and maghemite phases.⁴³ The bands in the range of $1370\text{--}1580\text{ cm}^{-1}$ are related to the magnetic properties of the iron oxide crystals, which may indicate the presence of maghemite since they are not encountered in the pure magnetite samples.^{43,44} The spectrum of the carbon nanotubes (Figure 3b) shows two characteristic bands, the G band located at 1580 cm^{-1} corresponding to the sp^2 bonds of the crystalline graphitic sheets, and the D band at 1354 cm^{-1} corresponding to defects of sp^3 bonds in the pentagonal and heptagonal carbon structures of the nanotubes.⁴⁵ The TiO₂

spectrum (Figure 3c) shows four characteristic bands of the anatase and rutile phases of TiO₂. The bands at 137 , 387 , 513 and 638 cm^{-1} correspond to the anatase phase and at 440 cm^{-1} to the rutile phase.^{45,46} The TiO₂-Ag-9 composite (Figure 3d) presented a new band at 90 cm^{-1} corresponding to the vibration mode of the Ag structure, moreover the band of TiO₂ at 137 cm^{-1} was shifted to 145 cm^{-1} due to the resonant Raman effect caused by deposition of Ag NPs on the TiO₂.⁴⁷ The phonon confinement can cause these changes to the Raman vibration mode and peak intensities.³⁷ Spectra of the MWCNT/TiO₂-Ag-9 and 10-Fe/MWCNT/TiO₂-Ag-9 composites are shown in Figures 3e and 3f. These spectra indicated the shift in wavenumbers and intensities of the D and G bands of the MWCNT from interaction with TiO₂-Ag and the iron oxide.

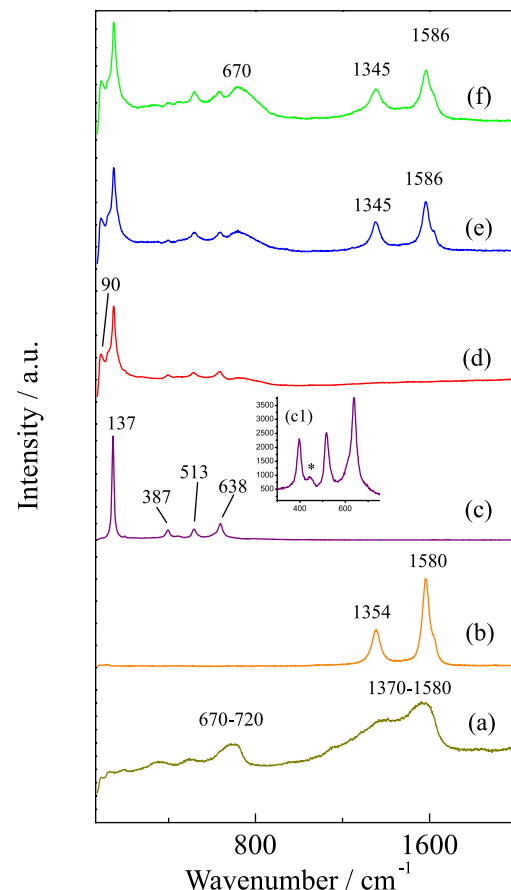


Figure 3. Raman spectra of (a) iron oxide, (b) MWCNT, (c) TiO₂, (c₁) expanded spectrum for TiO₂ range $300\text{--}750\text{ cm}^{-1}$ (*rutile phase of TiO₂), (d) TiO₂-Ag-9, (e) MWCNT/TiO₂-Ag-9 and (f) 10-Fe/MWCNT/TiO₂-Ag-9.

The G band of carbon nanotubes showed a shift of 6 cm^{-1} to blue and the D band of 9 cm^{-1} to red due to adhesion of the TiO₂-Ag on the surface of the carbon nanotubes.³⁷ The intensity ratio of the D and G bands of carbon nanotubes was $ID/IG = 0.4251$, for the composite

MWCNT/TiO₂-Ag-9 ID/IG = 0.7283 and for the composite 10-Fe/MWCNT/TiO₂-Ag-9 ID/IG = 0.6989. The increase of the intensity ratio is due to disturbances in the structure of the nanotubes by interaction with the TiO₂-Ag and iron oxide nanoparticles.⁴⁸ The presence of the TiO₂-Ag bands of the magnetite-maghemite and the shifts of the D and G bands of the carbon nanotubes (Figure 3f) indicated that there was a strong interaction between the catalyst components.

Determination of band-gap values

Figures 4a and 4b show the UV-Vis spectra of diffuse reflectance. The Kubelka-Munk function $F(R) = (1 - R)^2 / 2R$ (R is the reflectance) was used to calculate the band-gap energy of the catalysts.⁴⁹ The calculation of the band-gap energy (Figure 4b) was performed by extrapolating the line obtained in the regression of the linear portion of $[F(R)h\nu]^n$ ($n = 1/2$ for indirect gap) vs. energy ($h\nu$), where h is Planck's constant and ν the frequency of light.⁵⁰ The band-gap values for TiO₂, TiO₂-Ag-9, MWCNT/TiO₂-Ag-9, 10-Fe/MWCNT/TiO₂, 10-Fe/MWCNT/TiO₂-Ag-9 and iron oxide are 3.20, 3.05, 2.84, 2.52, 2.24 and 1.97 eV, respectively. The 10-Fe/MWCNT/TiO₂-Ag-9 catalyst showed light absorption shifted to the visible region. This shift is due to the electronic interaction of molecular orbitals between iron oxide (presenting a narrow band gap, 0.1 eV for magnetite and 2.2 eV for maghemite) and TiO₂ (3.2-3.3 eV), constructing a new molecular orbital and reducing the band difference. Similar phenomena were observed between graphene and TiO₂,⁵¹ carbon nanotubes and TiO₂,⁵² and TiO₂ and iron oxide.⁵³ The displacement of radiation absorption to the visible region is also due to MWCNTs which act as photogenerated electron acceptors and to the surface plasmon resonance of electrons present in the Ag⁰ nanoparticles.^{37,54}

Thus, the combination of iron oxide, Ag⁰ and MWCNT in the catalyst composition contributed to increase the absorption of the visible light by TiO₂. The photogenerated electrons in the conduction band and the valence band gaps of the TiO₂ may be trapped by the iron oxide, maintaining the electron-hole separation.⁵⁵ In the charge transfer process, the Fe³⁺ of iron oxide is reduced to Fe²⁺ by the electrons of the TiO₂ conduction band, the Fe²⁺ can be oxidized to Fe³⁺ and the generated electrons react with O₂ to produce the superoxide ion (O₂^{•-}).⁵⁵⁻⁵⁸ The Fe³⁺ of iron oxide can be oxidized by the TiO₂ valence band gap to form Fe⁴⁺ which reacts with ⁻OH ions to form [•]OH radicals.⁵⁶ Electron transfer may also occur directly from the TiO₂ conduction band to the Ag NPs. The Ag⁰ which has a higher working

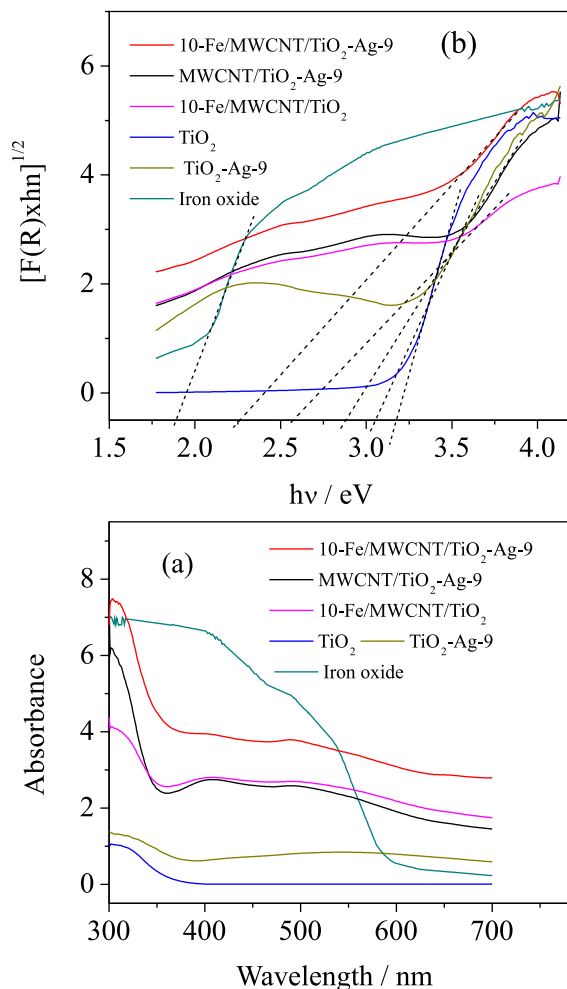


Figure 4. (a) UV-Vis absorption spectrum of the photocatalysts and (b) determination of band-gap values (E_g) for the photocatalysts.

function (4.26 eV) than that of TiO₂ (4.20 eV) can capture photogenerated electrons on TiO₂ and transfer them to MWCNTs, and these electrons can react with O₂ to form the radical O₂^{•-}.^{58,59} Thus, the effect of the interaction between the components of the catalyst increases the transport of electrons, prevents the recombination of charges and allows the use of visible radiation in the photodegradation of phenol.

Photocatalytic activity and kinetics

Figure 5 shows the results obtained in the phenol oxidation by varying the amounts of Ti, Ag and Fe added to the catalyst. In Figure 5a, it was verified that the photocatalyst which promoted the highest removal of phenol was that with a MWCNT:TiO₂-Ag ratio of 1:2 (12-MWCNT/TiO₂-Ag). Figure 5b shows that the maximum photodegradation efficiency was obtained by the catalyst with 9 wt.% Ag (0.000834 mol g⁻¹). The increase in wt.% of Ag improves the efficiency of the catalyst, but when reaching a silver content (> 9%), the opposite effect

occurred. The Ag nanoparticles increase the probability of electron capture by the valence band of TiO_2 , reducing the charge separation time and hence the photocatalytic efficiency.⁷ In Figure 5c, the highest photocatalytic efficiency was obtained by the catalyst with 10 wt.% Fe ($0.0018 \text{ mol g}^{-1}$). For larger amounts of Fe, the efficiency decreases. Larger quantities of Fe^{3+} decrease the surface area of the catalyst to prevent light penetration.^{60,61}

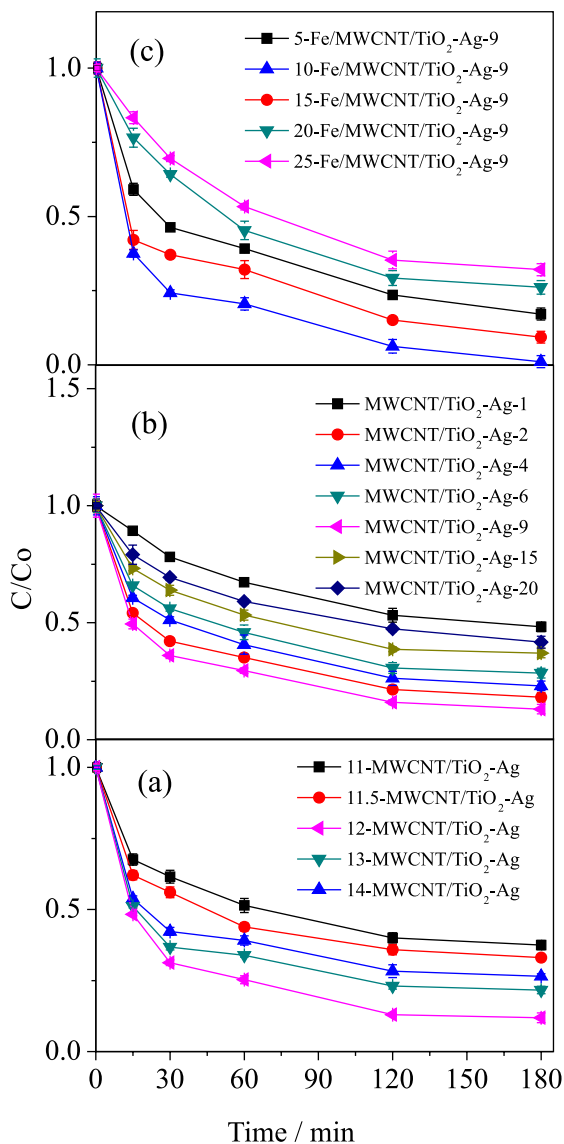


Figure 5. Photocatalytic activity of the catalysts: (a) with different amounts of TiO_2 -Ag, (b) with different amounts of Ag and (c) with different amounts of iron oxide for phenol degradation. Reaction conditions: initial phenol concentration of 50 mg L^{-1} , 300 mg of photocatalyst, reaction temperature $30 \pm 2 \text{ }^\circ\text{C}$ and initial pH 5.2.

Figure 6 shows the influence of pH on phenol photodegradation by 10-Fe/MWCNT/ TiO_2 -Ag-9 and determination of the point of zero charge (ZPC) for the catalysts. The ZPC values determined for TiO_2 and

MWCNT were 6.10 and 4.00, respectively, and are in agreement with values reported in the literature.^{4,62} The ZPC value of the 10-Fe/MWCNT/ TiO_2 -Ag-9 catalyst was 5.49 (Figure 6a), being that at values of $\text{pH} < \text{pH}_{\text{ZPC}}$, the catalyst surface is positively charged, and at $\text{pH} > \text{pH}_{\text{ZPC}}$, it is negatively charged. Figure 6b shows that the removal of phenol by the catalyst was highest in the pH range of 3.0 to 5.20 ($\text{pH} < \text{pH}_{\text{ZPC}}$), and at $\text{pH} > \text{pH}_{\text{ZPC}}$, there was a decrease in the removal of phenol.

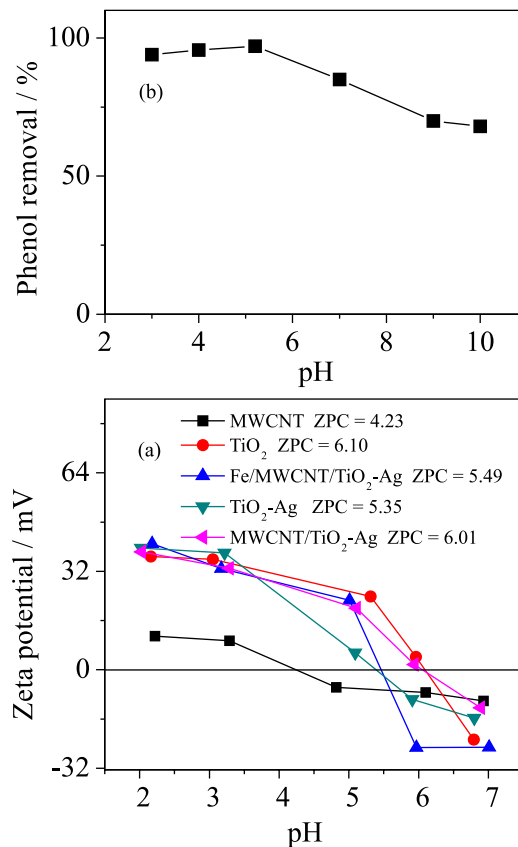


Figure 6. (a) Zeta potential measurements, (b) influence of pH on the removal of phenol by the catalyst 10-Fe/MWCNT- TiO_2 -Ag-9. Reaction conditions: initial phenol concentration of 50 mg L^{-1} , 300 mg of photocatalyst and reaction temperature $30 \pm 2 \text{ }^\circ\text{C}$.

At pH of 3.0 to 5.20 ($\text{pH} < \text{pH}_{\text{ZPC}}$), the catalyst surface is positively charged and the electron recombination rate with h_{VB}^+ holes is minimized by providing a greater photocatalytic activity. The presence of negative charges on the catalyst surface ($\text{pH} > \text{pH}_{\text{ZPC}}$) inhibits the adsorption of ^-OH ions and water molecules, and consequently decreases the amount of $^{\bullet}\text{OH}$ radicals formed, in addition to increasing the recombination rate of the electrons generated in the conduction band with valence band of TiO_2 .¹⁸ At pH above 9, carbonate is found in solution (formed by the absorption of CO_2 from the air), and reacts with ^-OH ions to diminish the production of $^{\bullet}\text{OH}$ radicals, reducing the

removal of phenol.⁶³ Phenol (pK_a = 9.95) at pH 9-10 is found in the form of phenoxide ion, which is repelled by the negative loads on the surface of the catalyst (pH > pH_{ZPC}), contributing to the decrease of the phenol removal rate.⁶⁴

A comparison of the various synthesized catalysts (Figure 7) shows a high efficiency for phenol photodegradation by 10-Fe/MWCNT/TiO₂-Ag-9 (ca. 100%). In studies on the absence of radiation, the phenol removal was assessed by adsorption.

In Figure 7a, it is observed that 10-Fe/MWCNT/TiO₂-Ag-9 adsorbed 7% of phenol after 180 min in the absence of UV-Vis radiation. The TOC removal was also quantified (Figure 7b) to measure the degree of phenol mineralization.

The catalyst 10-Fe/MWCNT/TiO₂-Ag-9, which resulted in the highest phenol removal (Figure 7a), also generated a greater reduction in TOC, reaching approximately 85% after 180 min. The TiO₂ catalyst when compared to TiO₂-Ag-9 generated an increase in the phenol photodegradation by 28 to 68%. The incorporation of Ag NPs in the 10-Fe/MWCNT-TiO₂ forming the 10-Fe/MWCNT/TiO₂-Ag-9 catalyst had an additive effect, increasing the amount of phenol removed from 79 to ca. 100%, respectively.

The schemes of photoactivation of the catalyst and phenol degradation are shown in Figure 8. One photon (hν) with energy greater than the band-gap energy of TiO₂ promotes the valence band electrons (VB) to the conduction band.⁶⁵ Ag NPs in contact with TiO₂ captured the photogenerated electrons (e⁻_{CB}), increasing the electron-hole separation and preventing recombination.⁵⁵

The process of transferring electrons (e⁻_{CB}) from TiO₂ to Ag NPs (equations 1 and 2) occurs spontaneously due to its Fermi level being greater than that of Ag NPs.⁶⁶ Electrons stored in Ag NPs are transferred to MWCNT, which acts as donors of these electrons to dissolved oxygen to form the radical ion superoxide (O₂^{•-}) (equation 3). This transforms into reactive oxygen species, such as [•]OH, HO₂[•] and H₂O₂.⁵⁸

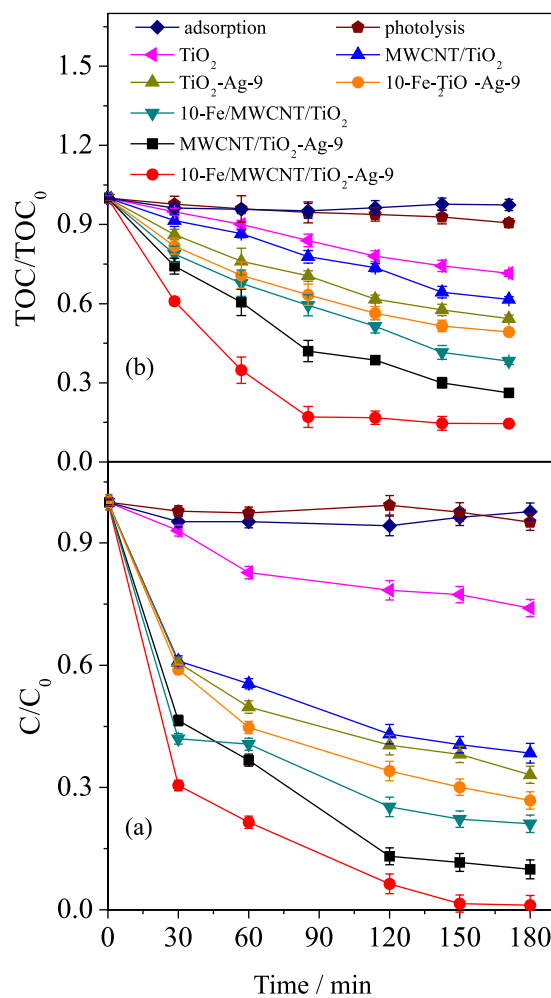


Figure 7. (a) Comparison of the photocatalytic activity of the catalysts for the removal of phenol, (b) variation in the total organic carbon content (TOC) of the solution during the phenol photodegradation. Reaction conditions: initial phenol concentration of 50 mg L⁻¹, 300 mg of photocatalyst, reaction temperature 30 ± 2 °C and initial pH 5.2.

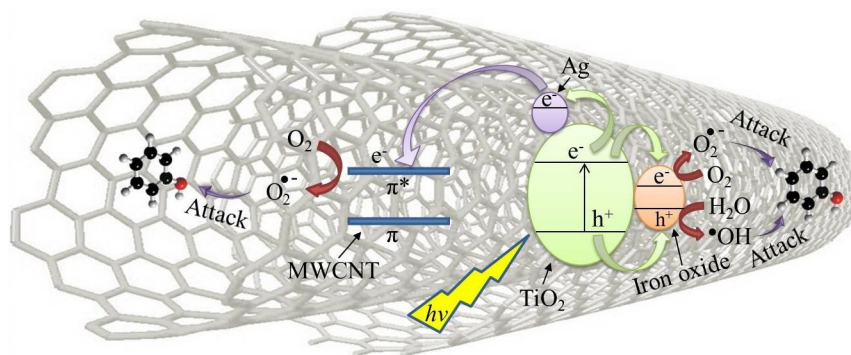


Figure 8. Proposal of the photocatalytic activation mechanism and phenol degradation.

The iron oxide present in the catalyst can act as a temporary site for capture of electrons (e_{CB}^-) and holes (h_{VB}^+) photogenerated on TiO_2 .^{55,67} Thus, the Fe^{3+} from iron oxide may act as a temporary photogenerator of electrons (equation 4) or in the capture of photogenerated electrons (equation 5), inhibiting the charge recombination of the TiO_2 .⁶⁷



Because Fe^{2+} and Fe^{4+} are more unstable than Fe^{3+} , there is a strong tendency for charge transfer of the TiO_2 surface to the iron oxide, forming the hydroxyl and superoxide radicals (equations 6 and 7).^{55,62,68}



The hydroxyl radicals and the superoxide anion produced in this process have sufficient oxidative potential to degrade phenol molecules (equations 8 and 9).

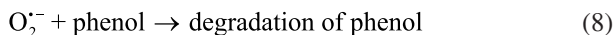


Table S1 (in the SI section) presents a summary of photocatalytic phenol degradation studies published in the literature. It can be observed that phenol degradation by 10-Fe/MWCNT/ TiO_2 -Ag-9 showed satisfactory performance compared to other catalysts previously reported.

Kinetics of phenol photodegradation

The photocatalytic reactions by degradation of organic pollutants follow pseudo-first-order model of Langmuir-Hinshelwood shown in equation 10.^{69,70}

$$r = -\frac{dC}{dt} = \frac{k_r K_{ad} C}{1 + K_{ad} C} \quad (10)$$

where r is degradation rate ($mg L^{-1} min^{-1}$), t the reaction time (min), C the concentration of the organic compound ($mg L^{-1}$), k_r the intrinsic rate constant and K_{ad} the adsorption equilibrium constant. At low initial organic compound concentrations and when adsorption is small, $K_{ad} C$ is negligible and the model is reduced to equation 11, where $K_{app} = k_r K_{ad}$ is the apparent rate constant.²⁵

$$\ln \frac{C_0}{C} = k_r K_{ad} t = K_{app} t \quad (11)$$

In this model, the slope of the $\ln(C_0/C)$ vs. time (t) plot is the apparent rate constant (K_{app}). Figure 9 presents results of phenol photodegradation kinetic studies that were used to determine apparent rate constants (K_{app}) and phenol half-lives ($t_{1/2}$). The half-life time ($t_{1/2}$) (the time at which $C = 0.5 C_0$) is one of the most useful values to compare pseudo-first-order reaction rates (equation 12):⁷¹

$$t_{1/2} = \frac{\ln 2}{K_{app}} \quad (12)$$

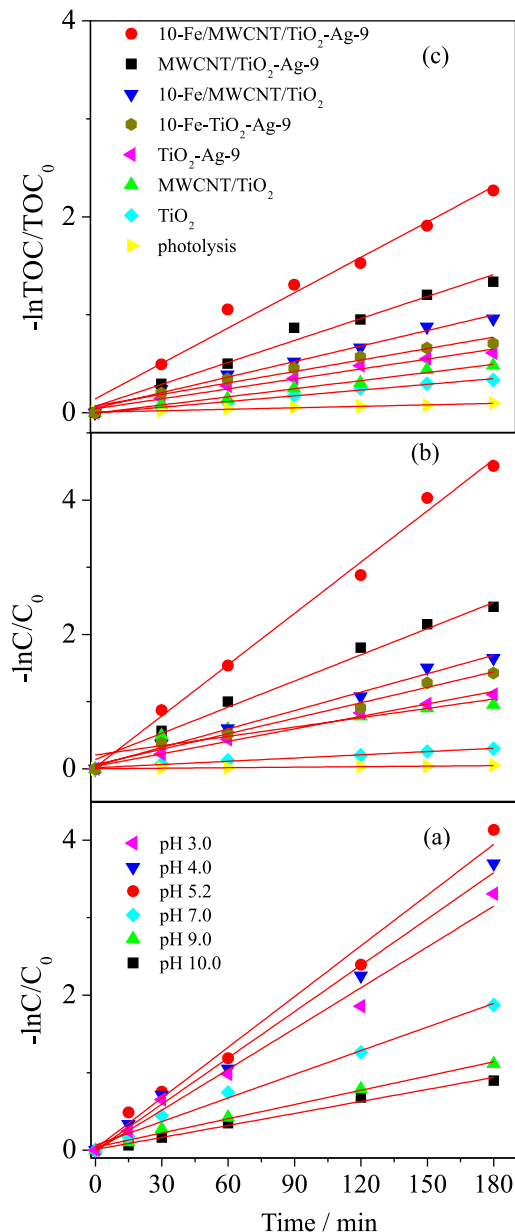


Figure 9. Pseudo-first-order degradation kinetics for phenol used to estimate Langmuir-Hinshelwood coefficients. Phenol removals: (a) with the catalyst 10-Fe/MWCNT/ TiO_2 -Ag-9 at various pH levels, (b) with different photocatalysts by HPLC-DAD and (c) TOC. Reaction conditions: initial phenol concentration of $50 mg L^{-1}$, 300 mg of photocatalyst and reaction temperature $30 \pm 2 ^\circ C$.

Table 2. Langmuir-Hinshelwood apparent rate constants (K_{app}), half-life ($t_{1/2}$) and coefficients of determination (R^2) for the photodegradation of phenol measured by HPLC-DAD and TOC

	HPLC-DAD ^a			TOC ^b		
	$K_{app} / \text{min}^{-1}$	$t_{1/2} / \text{min}$	R^2	$K_{app} / \text{min}^{-1}$	$t_{1/2} / \text{min}$	R^2
Photolysis	0.0005	1414.6	0.983	0.0003	2682.2	0.992
TiO ₂	0.0020	355.5	0.989	0.0016	430.5	0.976
TiO ₂ -Ag-9	0.0062	111.9	0.999	0.0034	203.9	0.987
10-Fe-TiO ₂ -Ag-9	0.0077	90.1	0.982	0.0039	177.7	0.975
MWCNT-TiO ₂	0.0032	216.6	0.992	0.0028	247.6	0.988
10-Fe/MWCNT/TiO ₂	0.0092	75.8	0.989	0.0053	130.8	0.978
MWCNT/TiO ₂ -Ag-9	0.0130	53.4	0.989	0.0075	92.4	0.979
10-Fe/MWCNT/TiO ₂ -Ag-9	0.0255	27.2	0.982	0.0120	57.8	0.978

^aHPLC-DAD: high performance liquid chromatography with linear photodiode array detector; ^bTOC: total organic carbon.

The kinetic data for pH variation (Figure 9a), phenol photodegradation by HPLC-DAD (Figure 9b) and TOC photodegradation (Figure 9c) results adjusted well to the pseudo-first-order kinetic model, with coefficients of determination (R^2) higher than 0.97.

Apparent rate constants (K_{app}), half-life times ($t_{1/2}$) and the coefficients of determination (R^2) are summarized in Tables 2 and S2 (in the SI section).

Figure 9a and Table S2 show that the highest phenol photodegradation rate is between pH 3.00-5.20 ($K_{app} = 0.018$ to 0.025 min^{-1} and $t_{1/2} = 38.5$ to 27.7 min), and the smallest photodegradation rates occur at pH levels exceeding 5.2. The values obtained for pH 7 and 10 are $K_{app} = 0.012$ and 0.006 min^{-1} , and $t_{1/2} = 57.8$ and 115.5 min , respectively. The degradation rate is influenced by the solution pH, where the lowest rates are at $\text{pH} > \text{pH}_{ZPC}$ ($\text{pH}_{ZPC} > 5.49$) for the catalyst.

In Figures 9b and 9c, when comparing the TiO₂ reaction rates with other catalysts, it is clear that the incorporation of MWCNT, Fe and TiO₂-Ag in preparation of the catalyst 10-Fe/MWCNT/TiO₂-Ag-9 promoted an improvement in the kinetics of phenol photodegradation.

There was an increase in the reaction speed of 12.5 times with K_{app} (TiO₂) = 0.0020 min^{-1} to K_{app} (10-Fe/MWCNT/TiO₂-Ag-9) = 0.0255 min^{-1} . Half-lives of 216.6 min (phenol by HPLC-DAD) and 247.6 min (TOC) were found for the photodegradation with the MWCNT-TiO₂ composite. The incorporation of Fe or Ag on MWCNT/TiO₂ increased the reaction rate, with half-life for 10-Fe/MWCNT/TiO₂ and MWCNT/TiO₂-Ag-9 of 75.8 and 53.4 min (phenol by HPLC-DAD), and 130.8 and 92.4 min (TOC), respectively. The simultaneous incorporation of Fe and Ag on MWCNT-TiO₂ forming the composite 10-Fe/MWCNT/TiO₂-Ag-9 reduces the half-lives to 27.2 min (phenol by HPLC-DAD) and

57.8 min (TOC), corresponding to $K_{app} = 0.0255 \text{ min}^{-1}$ (phenol by HPLC-DAD) and 0.0120 min^{-1} (TOC). Wang *et al.*²⁷ reported phenol photodegradation by 20-MWCNT-TiO₂ of 96% (initial concentration of 50 mg L^{-1}) after 5 h with $K_{app} = 0.0074 \text{ min}^{-1}$ and $t_{1/2} = 93 \text{ min}$. Almeida *et al.*²⁵ evaluated phenol degradation (initial concentration of 50 mg L^{-1}) by TiO₂/MgZnAl-5 after 6 h, with $K_{app} = 0.0114 \text{ min}^{-1}$ and $t_{1/2} = 60.8 \text{ min}$. In the study by Chiou *et al.*⁷⁰ using TiO₂ P-25, a phenol degradation of 84% was reported (initial concentration of 50 mg L^{-1}) in 3 h with $K_{app} = 0.014 \text{ min}^{-1}$ and $t_{1/2} = 49.3 \text{ min}$ using a 400 W UV lamp and addition of H₂O₂ (0.05 mg L^{-1}). Therefore, one can conclude that the 10-Fe/MWCNT/TiO₂-Ag-9 composite photocatalyst showed satisfactory kinetic performance with the potential to eliminate phenolic compounds in an aqueous medium.

Reuse

For the purpose of practical application, it is necessary to evaluate the reuse and stability of the catalyst. The reuse studies were performed with recovery of the material (300 mg), maintaining constant all other parameters. Thus, the efficiency of 10-Fe/MWCNT/TiO₂-Ag-9 was evaluated by 10 reuse tests lasting 3 h each, totaling 30 h of study. The results showed that the catalyst presented good photocatalytic activity even after ten consecutive cycles. The yield for degradation of phenol was 100% in the first test and decreased to 92% in the tenth test (final test). Thus, the 10-Fe/MWCNT/TiO₂-Ag-9 catalyst remained stable, presenting an 8% decrease in phenol degradation efficiency after ten consecutive photocatalytic cycles.

Electron microscopy (Figure S2d), energy dispersive spectroscopy (Figure S3d), X-ray diffraction (Figure 1f) and infrared spectroscopy (Figure 2e) were used to evaluate

the stability of the catalyst. The results showed that there was no change in the chemical/physical characteristics of the 10-Fe/MWCNT/TiO₂-Ag-9 catalyst after ten consecutive photocatalytic cycles.

Conclusions

A magnetically recoverable catalyst, 10-Fe/MWCNT/TiO₂-Ag-9, was successfully synthesized in this work. The photocatalysts were used in UV-Vis (cut off filter > 300 nm) photodegradation of phenol in aqueous solution and presented high photocatalytic activity. The 10-Fe/MWCNT/TiO₂-Ag-9 composite photocatalyst resulted in approximately 100% phenol and 85% TOC removal from an aqueous phenol solution of initial concentration equal to 50 mg L⁻¹, after 180 min.

The 10-Fe/MWCNT/TiO₂-Ag-9 catalyst showed good stability after 10 cycles, thus showing promising potential for practical applications. Phenol removal with the novel catalyst was greater than that obtained with commercial TiO₂ (Degussa P25) because of its smaller band-gap energy (2.24 eV vs. 3.20 eV) and lower electron-hole pair recombination rate due to the presence of silver, iron oxide and MWCNT. Since the 10-Fe/MWCNT/TiO₂-Ag-9 photocatalyst shifted light absorption to a higher wavelength, less energy was required for photocatalytic activity and the phenol removal efficiency increased. Moreover, iron oxide makes the catalyst magnetic, so that, it is easily separated from the solution by applying an external magnetic field. The new photocatalysts showed a combined effect of the MWCNT support, the presence of iron oxide associated to the TiO₂-Ag photoactivity, resulting in formation of a composite with high photocatalytic capacity.

Supplementary Information

Supplementary data (annular photoreactor, SEM, EDS, photodegradation of phenol by catalysts with supported TiO₂ and Langmuir-Hinshelwood apparent rate constants) are available free of charge at <http://jbcns.sbq.org.br> as PDF file.

Acknowledgments

The authors acknowledge the financial support of the Fundação de Amparo à Pesquisa do Estado de Minas Gerais (FAPEMIG, Universal Demand, process No. APQ-00445-14) and the Conselho Nacional de Desenvolvimento Científico e Tecnológico (CNPq). We also thank the Laboratory of Nanomaterials of the DF/UFMG for providing the multi-walled carbon nanotubes.

References

1. Fox, M. A.; Dulay, M. T.; *Chem. Rev.* **1993**, *93*, 341.
2. Liu, J.; Bai, H.; Wang, Y.; Liu, Z.; Zhang, X.; Sun, D. D.; *Adv. Funct. Mater.* **2010**, *20*, 4175.
3. Almeida, L. C.; Zanoni, M. V. B.; *J. Braz. Chem. Soc.* **2014**, *25*, 579.
4. Ouyang, K.; Xie, S.; Ma, X.; *Ceram. Int.* **2013**, *39*, 7531.
5. Gui, M. M.; Wong, W. M. P.; Chai, S.-P.; Mohamed, A. R.; *Chem. Eng. J.* **2015**, *278*, 272.
6. Devi, L. G.; Nagaraj, B.; Rajashekhar, K. E.; *Chem. Eng. J.* **2012**, *181-182*, 259.
7. Sobana, N.; Selvam, K.; Swaminathan, M.; *Sep. Purif. Technol.* **2008**, *62*, 648.
8. Stropa, J. M.; Herrero, A. S.; Oliveira, S. C.; Cavalheiro, A. A.; Dantas, F.; Oliveira, S. L.; Oliveira, L. C. S.; *J. Braz. Chem. Soc.* **2016**, *27*, 575.
9. Luo, Y.; Lu, Z.; Jiang, Y.; Wang, D.; Yang, L.; Huo, P.; Da, Z.; Bai, X.; Xie, X.; Yang, P.; *Chem. Eng. J.* **2014**, *240*, 244.
10. Woan, B. K.; Pyrgiotakis, G.; Sigmund, W.; *Adv. Mater.* **2009**, *21*, 2233.
11. Ou, Y.; Lin, J.; Fang, S.; Liao, D.; *Chem. Phys. Lett.* **2006**, *429*, 199.
12. Gui, M. M.; Chai, S. P.; Xu, B. Q.; Mohamed, A. R.; *Sol. Energy Mater. Sol. Cells* **2014**, *122*, 183.
13. Xin, T.; Ma, M.; Zhang, H.; Gu, J.; Wang, S.; Liu, M.; Zhang, Q.; *Appl. Surf. Sci.* **2014**, *288*, 51.
14. Zhou, H.; Zhang, C.; Wang, X.; Li, H.; Du, Z.; *Synth. Met.* **2011**, *161*, 2199.
15. Etacheri, V.; Di Valentin, C.; Schneider, J.; Bahnemann, D.; Pillai, S. C.; *J. Photochem. Photobiol., C* **2015**, *25*, 1.
16. Luo, Y.; Lu, Z.; Yinhu, J.; Wang, D.; Yang, L.; Huo, P.; Da, Z.; Bai, X.; Xie, X.; Yang, P.; *Chem. Eng. J.* **2014**, *240*, 244.
17. Zhang, P.; Mo, Z.; Han, L.; Wang, Y.; Zhao, G.; Zhang, C.; *J. Mol. Catal. A: Chem.* **2015**, *402*, 17.
18. Aguilar, C. A. H.; Pandiyan, T.; Arenas-Alatorre, J. A.; Singh, N.; *Sep. Purif. Technol.* **2015**, *149*, 265.
19. Yin, H.; Dai, X.; Zhu, M.; Li, F.; Feng, X.; Liu, F.; *J. Hazard. Mater.* **2015**, *296*, 221.
20. Toledo, T. V.; Bellato, C. R.; do Rosário, R. H.; Marques Neto, J. O.; *Quim. Nova* **2011**, *34*, 561.
21. Devi, L. G.; Reddy, K. M.; *Appl. Surf. Sci.* **2011**, *257*, 6821.
22. Lin, K. N.; Liou, W. J.; Yang, T. Y.; Lin, H. M.; Lin, C. K.; Chien, S. H.; Chen, W. C.; Wu, S. H.; *Diamond Relat. Mater.* **2009**, *18*, 312.
23. Zhou, D.; Ding, L.; Cui, H.; An, H.; Zhai, J.; Li, Q.; *J. Power Sources* **2013**, *222*, 510.
24. Wang, X.; Wu, P.; Lu, Y.; Huang, Z.; Zhu, N.; Lin, C.; Dang, Z.; *Sep. Purif. Technol.* **2014**, *132*, 195.
25. Almeida, F. M.; Bellato, R. C.; Honor, A.; Olavo, S.; Milagres, L. J.; Miranda, D. L. L.; *Appl. Surf. Sci.* **2015**, *357*, 1765.

26. Li, H.; Ma, Y.; Niu, R.; *Sep. Purif. Technol.* **2016**, *171*, 93.
27. Wang, W.; Serp, P.; Kalck, P.; Lu, J.; *J. Mol. Catal. A: Chem.* **2005**, *235*, 194.
28. Rather, S.; Mehrajuddin, N.; Zacharia, R.; Hwang, S. W.; Kim, A. R.; Nahm, K. S.; *Int. J. Hydrogen Energy* **2009**, *34*, 961.
29. Ai, L.; Jiang, J.; *Chem. Eng. J.* **2012**, *192*, 156.
30. Quiñones, D. H.; Rey, A.; Álvarez, P. M.; Beltrán, F. J.; Plucinski, P. K.; *Appl. Catal., B* **2014**, *144*, 96.
31. Kim, C.; *J. Ind. Eng. Chem. (Amsterdam, Neth.)* **2015**, *31*, 43.
32. Wang, H.; Cao, L.; Yan, S.; Huang, N.; Xiao, Z.; *Mater. Sci. Eng., B* **2009**, *164*, 191.
33. Miranda, L. D. L.; Bellato, C. R.; Milagres, J. L.; Moura, L. G.; Mounteer, A. H.; de Almeida, M. F.; *J. Environ. Manage.* **2015**, *156*, 225.
34. Aysin, B.; Ozturk, A.; Park, J.; *Ceram. Int.* **2013**, *39*, 7119.
35. Yang, Y.; Liu, E.; Dai, H.; Kang, L.; Wu, H.; *Int. J. Hydrogen Energy* **2013**, *39*, 7664.
36. Pugazhenthiran, N.; Murugesan, S.; Anandan, S.; *J. Hazard. Mater.* **2013**, *263*, 541.
37. Koo, Y.; Littlejohn, G.; Collins, B.; Yun, Y.; Shanov, V. N.; Schulz, M.; Pai, D.; Sankar, J.; *Composites Part B* **2014**, *57*, 105.
38. Aazam, E. S.; *Ceram. Int.* **2014**, *40*, 6705.
39. Stéfani, D.; Paula, A. J.; Vaz, B. G.; Silva, R. A.; Andrade, N. F.; Justo, G. Z.; Ferreira, C. V.; Filho, A. G. S.; Eberlin, M. N.; Alves, O. L.; *J. Hazard. Mater.* **2011**, *189*, 391.
40. Saleh, T. A.; Gupta, V. K.; *J. Colloid Interface Sci.* **2011**, *362*, 337.
41. Anbarasu, M.; Anandan, M.; Chinnasamy, E.; Gopinath, V.; Balamurugan, K.; *Spectrochim. Acta, Part A* **2015**, *135*, 536.
42. Zhang, X.; Lei, L.; *J. Hazard. Mater.* **2008**, *153*, 827.
43. Froment, F.; Tourmié, A.; Colomban, P.; *J. Raman Spectrosc.* **2008**, *39*, 560.
44. Neff, D.; Ludovic, B.-G.; Philippe, D.; Solen, R.; Ludovic, L.; *J. Raman Spectrosc.* **2007**, *38*, 1538.
45. Ma, L.; Chen, A.; Lu, J.; Zhang, Z.; He, H.; Li, C.; *Particuology* **2014**, *14*, 24.
46. Nossol, A. B. S.; Suzamar, M. C. R. S.; Nossol, E.; Zarbin, A. J. G.; Peralta-Zamora, P.; *Quim. Nova* **2016**, *10*, 1.
47. Jaafar, N. F.; Jalil, A. A.; Triwahyono, S.; Efendi, J.; Mukti, R. R.; Jusoh, R.; Jusoh, N. W. C.; Karim, A. H.; Salleh, N. F. M.; Suendo, V.; *Appl. Surf. Sci.* **2015**, *338*, 75.
48. Gao, B.; Jiang, Z.; Zhao, C.; Gomaa, H.; Pan, F.; *J. Membr. Sci.* **2015**, *492*, 230.
49. Choudhury, B.; Choudhury, A.; *Mater. Chem. Phys.* **2012**, *132*, 1112.
50. Calandra, P.; Lombardo, D.; Pistone, A.; Liveri, V. T.; Trusso, S.; *J. Nanopart. Res.* **2011**, *13*, 5833.
51. Liu, S. S.; Sun, H.; Liu, S. S.; Wang, S.; *Chem. Eng. J.* **2013**, *214*, 298.
52. Sampaio, M. J.; Silva, C. G.; Marques, R. R. N.; Silva, A. M. T.; Faria, J. L.; *Catal. Today* **2011**, *161*, 91.
53. Tang, Y.; Zhang, G.; Liu, C.; Luo, S.; Xu, X.; Chen, L.; Wang, B.; *J. Hazard. Mater.* **2013**, *252-253*, 115.
54. He, J.; Ichinose, I.; Kunitake, T.; Nakao, A.; *Langmuir* **2002**, *18*, 10005.
55. Harifi, T.; Montazer, M.; *Ultrason. Sonochem.* **2015**, *27*, 543.
56. Harifi, T.; Montazer, M.; *Appl. Catal., A* **2014**, *473*, 104.
57. Jia, X.; Dai, R.; Lian, D.; Han, S.; Wu, X.; Song, H.; *Appl. Surf. Sci.* **2017**, *392*, 268.
58. Ghavami, M.; Mohammadi, R.; Koohi, M.; Kassaee, M. Z.; *Mater. Sci. Semicond. Process.* **2014**, *26*, 69.
59. Tang, Y.; Luo, S.; Teng, Y.; Liu, C.; Xu, X.; Zhang, X.; Chen, L.; *J. Hazard. Mater.* **2012**, *241-242*, 323.
60. Yeh, N.; Lee, Y. C.; Chang, C. Y.; Cheng, T. C.; *Thin Solid Films* **2013**, *549*, 93.
61. Lu, Z.; Chen, F.; He, M.; Song, M.; Ma, Z.; Shi, W.; Yan, Y.; Lan, J.; Li, F.; Xiao, P.; *Chem. Eng. J.* **2014**, *249*, 15.
62. Yu, J.; Yu, H.; Ao, C. H.; Lee, S. C.; Yu, J. C.; Ho, W.; *Thin Solid Films* **2006**, *496*, 273.
63. McManamon, C.; Holmes, J. D.; Morris, M.; *J. Hazard. Mater.* **2011**, *193*, 120.
64. Khraisheh, M.; Wu, L.; Al-Muhtaseb, A. H.; Albadarin, A. B.; Walker, G. M.; *Chem. Eng. J.* **2012**, *213*, 125.
65. Nogueira, R. F. P.; Jardim, W. F.; *Quim. Nova* **1998**, *2*, 69.
66. Sclafani, A.; Herrmann, J.-M.; *J. Photochem. Photobiol., A* **1998**, *113*, 181.
67. Zhao, W.; Zhang, J.; Zhu, X.; Zhang, M.; Tang, J.; Tan, M.; Wang, Y.; *Appl. Catal., B* **2014**, *144*, 468.
68. Liu, W.; Zhao, X.; Borthwick, A. G. L.; Wang, Y.; Ni, J.; *ACS Appl. Mater. Interfaces* **2015**, *17*, 19726.
69. Liu, W.; Ni, J.; Yin, X.; *Water Res.* **2014**, *53*, 12.
70. Chiou, C.; Wu, C.; Juang, R.; *Chem. Eng. J.* **2008**, *139*, 322.
71. Shaban, Y. A.; El Sayed, M. A.; El Maradny, A. A.; Al Farawati, R. Kh.; Al Zobidi, M. I.; *Chemosphere* **2013**, *91*, 307.
72. Grabowska, E.; Sobczak, J. W.; Gazda, M.; Zaleska, A.; *Appl. Catal., B: Environ.* **2012**, *117-118*, 351.
73. Ling, H.; Kim, K.; Liu, Z.; Shi, J.; Zhu, X.; Huang, J.; *Catal. Today* **2015**, *258*, 96.
74. Mohamed, M. A.; Salleh, W. N. W.; Jaafar, J.; Ismail, A. F.; Nor, N. A. M.; *Mater. Chem. Phys.* **2015**, *162*, 113.
75. Murcia, J. J.; Hidalgo, M. C.; Navío, J. A.; Araña, J.; Doña-Rodríguez, J. M.; *Appl. Catal., B: Environ.* **2015**, *179*, 305.
76. Qiu, R.; Zhang, D.; Diao, Z.; Huang, X.; He, C.; Morel, J.-L.; Xiong, Y.; *Water Res.* **2012**, *46*, 2299.
77. Andrade, M. A.; Carmona, R. J.; Mestre, A. S.; Matos, J.; Carvalho, A. P.; Ania, C. O.; *Carbon* **2014**, *76*, 183.

Submitted: March 3, 2017

Published online: May 5, 2017